

Classifying bacteria clones using attention-based deep multiple instance learning interpreted by persistence homology

Adriana Borowa^{1,2}, Dawid Rymarczyk^{1,2}, Dorota Ochońska³, Monika Brzychczy-Włoch⁴, and Bartosz Zieliński^{1,2,*}

¹Faculty of Mathematics and Computer Science, Jagiellonian University, 6 Łojasiewicza Street, 30-348 Kraków, Poland,

²Ardigen SA, 76 Podole Street, 30-394 Kraków, Poland,

³Department of Infection Epidemiology, Chair of Microbiology, Faculty of Medicine, Jagiellonian University Medical College, 18 Czysta Street, 31-121 Kraków, Poland

⁴Department of Bacteriology, Microbial Ecology and Parasitology, Chair of Microbiology, Jagiellonian University Medical College, 18 Czysta Street, 31-121 Kraków, Poland

*bartosz.zielinski@uj.edu.pl

Abstract

In this work, we analyze if it is possible to distinguish between different clones of the same bacteria species (*Klebsiella pneumoniae*) based only on microscopic images. It is a challenging task, previously considered impossible due to the high clones' similarity. For this purpose, we apply a multi-step algorithm with attention-based multiple instance learning. Except for obtaining accuracy at the level of 0.9, we introduce extensive interpretability based on CellProfiler and persistence homology, increasing the understandability and trust in the model.

1. Introduction

Genotyping bacteria clones is a crucial part of epidemiological management because it helps to assess the infection source in a hospital and prevent new cases. There exists several techniques to differentiate between bacteria clones, such as ribotyping [1], amplified fragment length polymorphism [11], multilocus sequence typing [3], and the most widely used pulsed-field gel electrophoresis [7, 14, 15]. However, all of them require costly equipment and reagents, and are highly unstable. Therefore, they must be repeated many times to obtain reliable results.

In this paper, we analyze if it is possible to distinguish between different clones of the same bacteria specie based only on microscopic images. We introduce a database containing 3 clones with 32 isolates of *Klebsiella pneumoniae*,

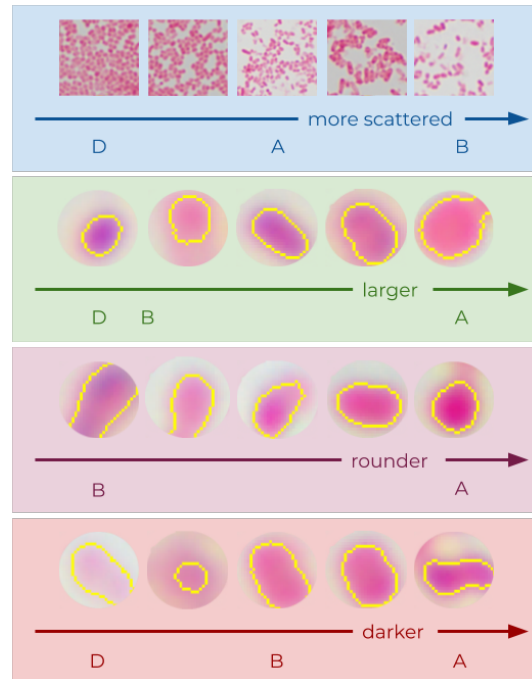


Figure 1: Summary of statistically significant differences in scattering (blue arrows), size (green arrows), roundness (purple arrows), and darkness (red arrows) between the clones A, B, and D of *Klebsiella pneumoniae* based on the results presented in Section 6.

a Gram-negative rod-shaped bacteria that may cause pneumonia, urinary tract infections or even sepsis [6, 12, 13].

Due to the large resolution of microscopic images, before classification, we first divide an image into patches, then generate their representations, and finally apply attention-based multiple instance learning, AbMIL [10]. AbMIL aggregates representations using the attention mechanism that promotes the essential patches. Therefore, except for the classification results, it also returns the attention scores that correspond to the patches' importance. Patches with the highest scores can be used to interpret results obtained for a specific image. However, they do not provide the clones' systematic characteristics, neither from the spatial arrangement nor from the individual cell perspective. At the same time, this characteristic is necessary to trust the model because microbiologists commonly assume that differentiating the clones of the same bacteria type based only on microscopic images is impossible.

To effectively interpret the AbMIL, we introduce two methods based on the essential patches segmented using CellProfiler [2]. The first one, based on persistence homology [4], analyzes the spatial arrangement of the bacteria, while the second one examines the size, shape, and color of the individual cells. According to microbiologists, both methods deliver a convincing explanation of the obtained results and increase the trust in the model.

To the best of our knowledge, it is the first attempt to distinguish between different clones of the same bacteria specie. Previous works either tried to recognize bacteria morphology or distinguish between different bacteria species [20], which is a much simpler task. The main contributions of this paper are as follows:

- Differentiating between bacteria clones based only on microscopic images (task previously considered impossible) at 0.9 level of accuracy.
- Applying persistence homology to explain differences in the spatial arrangement of bacteria between the analyzed clones.
- Delivering a convincing explanation of the obtained results on the level of individual cells.
- Introducing a publicly available database containing 3 clones with 32 isolates of *Klebsiella pneumoniae*.

2. DIBaC database

We introduce the Digital Images of Bacteria Clones (DIBaC) dataset. It contains 3 clones of *Klebsiella pneumoniae* further described as clones *A*, *B*, and *D*, containing 11, 10, and 11 isolates, respectively. Each isolate is represented by a set of 20 images from 2 preparations (10 images per preparation) to minimize the environmental bias. Isolates were obtained from patients of one hospital and come

from the respiratory tract, urine, wound swabs, blood, fecal samples, catheter JJ, and urethral swab. All of the samples were Gram-stained and analyzed using an Olympus XC31 Upright Biological Microscope equipped with an Olympus SC30 camera to present Gram-negative organisms. They were photographed using Olympus D72 with 12 bit image depth and saved as TIFF images of size 3500×5760 pixels. Sample images from DIBaC are presented in Fig. 12. The database is publicly available.¹

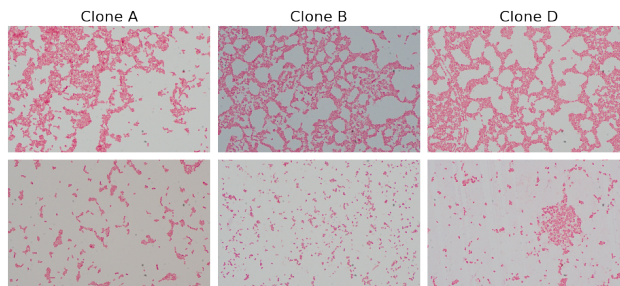


Figure 2: Sample images from the DIBaC database (2 per clone). See supplementary materials for more samples.

To cluster considered isolates into the clones, they were analyzed using pulsed-field gel electrophoresis (PFGE), a gold standard that relies on separating the DNA fragments after restriction cutting. PFGE profiles of the isolates were then interpreted using GelCompar software² to obtain a dendrogram calculated with the Dice (band-based similarity) coefficient. According to the dendrogram presented in Fig. 3, isolates cluster to three clones. Clones *A* and *B* are similar (identity at the level of 92%), while clone *D* is more different from the others (identity at the level of 77%). We use clones returned by GelCompar as the ground truth.

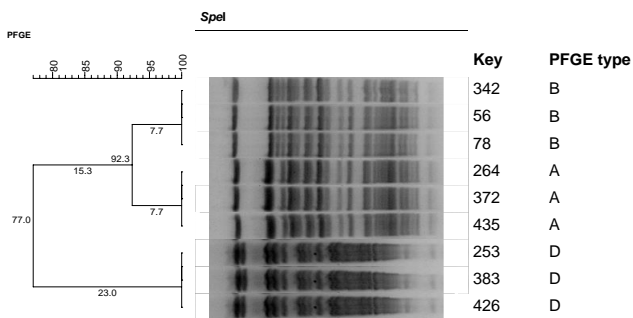


Figure 3: Dendrogram calculated for 9 isolates of *Klebsiella pneumoniae* (3 per clone) based on GelCompar software. This figure limits the original number of 32 isolates to 9 for paper clarity.

¹We will add the link to the database after paper acceptance.

²<https://www.applied-maths.com/gelcompar-ii>

3. Method

The pipeline of our method consists of multiple steps (see Fig. 4). Firstly, the image is divided into patches. Then, the foreground patches are preprocessed and passed through the patches representation network. Obtained representations are then aggregated using attention-based multiple instance learning [9] to obtain one fixed-sized vector for each image. Finally, such a vector can be passed to the successive fully-connected (FC) layers of the network to classify the bacteria’s clone. Due to the large number of patches per image, it is impossible to train the model at once. Therefore, we divided it into separately trained representation and classification networks. We describe them below, together with the preprocessing step.

Generating patches and preprocessing. Each image is scaled by a factor of 0.5 and divided into the patches of resolution 250×250 pixels using sliding window with stride 125 (the optimal scale, resolution, and stride were obtained from preliminary experiments). The background patches (with no bacteria) are then filtered out by rejecting those with standard deviation of the grayscale version smaller than 1.5. The remaining foreground patches are normalized using the mean and the standard deviation computed based on 10000 random training patches.

Patch representation network. Normalized patches are passed through ResNet-18 network [8] pre-trained on ImageNet and then finetuned with the last layer replaced by two neurons corresponding to two considered clones (according to the preliminary experiment, a version without finetuning resulted in poor accuracy). The training was performed for all layers of the network, with weighted sampling to reduce the influence of data imbalance, and with cross-entropy loss function. Training images were augmented using color jittering, random rotation, and random flip. The representations of the patches are obtained by taking the penultimate layer’s output.

Image classification network. To aggregate patches’ representations of an image, we apply attention-based multiple instance learning, AbMIL [10, 17], a type of weighted average pooling, where the neural network determines the weights of representations. More formally, if $\mathbf{h} = \{\mathbf{h}_i\}_{i=1}^N$, $\mathbf{h}_i \in \mathbb{R}^{L \times 1}$ is the set of patches’ representations of an image, then the output of the operator is defined as:

$$\mathbf{z} = \sum_{i=1}^N a_i \mathbf{h}_i, \text{ where } a_i = \frac{\exp(\mathbf{w}^T \tanh(\mathbf{V}\mathbf{h}_i))}{\sum_j \exp(\mathbf{w}^T \tanh(\mathbf{V}\mathbf{h}_j))}, \quad (1)$$

$\mathbf{w} \in \mathbb{R}^{M \times 1}$ and $\mathbf{V} \in \mathbb{R}^{M \times L}$ are trainable layers of neural networks and the weights a_i sum up to 1 to make the model

independent from various sizes of \mathbf{h} . Aggregated vector \mathbf{z} is further processed by a dense layer with two output neurons.

4. Interpretability

To interpret what properties of bacteria are important for the AbMIL when distinguishing between two clones, we create a set of essential patches that contains two patches with the highest attention weight (a_i value) from each correctly classified training image. We decided to analyze such a set because it includes patches with the greatest influence on the results. Therefore, they are the best choice when it comes to presenting what is important for the image classification network.

We apply two types of analysis. The first one, based on persistence homology [4], analyzes the spatial arrangement of the bacteria, while the second one examines the size, shape, and color of the individual cells. Both of them are preceded by bacteria cells’ segmentation obtained with CellProfiler [2] with a pipeline describe below.

Segmentation of bacteria. To segment bacteria, we first transform a patch into the grayscale image and then apply a CellProfiler with only one component identifying primary objects with a typical diameter of objects between 10 and 40 pixels³. The objects outside the diameter range are discarded as well as the objects touching the border. The result of segmentation for sample patches is presented in Fig. 5.

Spatial arrangement of bacteria. For each segmentation of a patch, we generate a point cloud $C \subset \mathbb{R}^2$ containing centers of the segmented bacteria and analyze this point cloud using persistence homology [4], that provides a comprehensive, multiscale summary of the underlying data’s shape and is currently gaining increasing importance in data science [5].

PH can be defined for a continuous function $f : C \rightarrow \mathbb{R}$, typically a distance function from a collection of points (in this case, centers of the bacteria). Focusing on sub-level sets $L_c = f^{-1}((-\infty, c])$, we let c grow from $-\infty$ to $+\infty$. While this happens, we can observe a hierarchy of events (see Fig. 6). In dimension 0, connected components of L_c are created and merged. In dimension 1, cycles that are not bounded or higher dimensional voids appear in L_c at critical points of f . The value of c on which a connected component, cycle, or a higher dimensional void, appears is referred to as *birth time*. They subsequently either become identical (up to a deformation) to other cycles and voids (created earlier) or glued-in and become trivial. The value of c on which that happens is referred to as *death time*. As

³For details, see <http://cellprofiler-manual.s3.amazonaws.com/CellProfiler-3.0.0/modules/objectprocessing.html#identifyprimaryobjects>

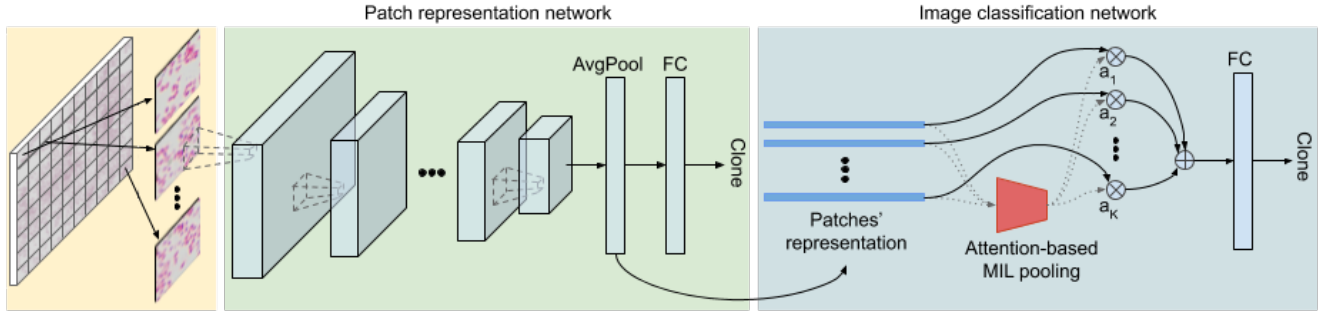


Figure 4: The pipeline of the method: (i) the image is divided into patches; (ii) the foreground patches are preprocessed and passed through the representation network; (iii) patches' representations are aggregated with AbMIL to obtain one fixed-sized vector for each image; (iv) the vector is passed to the fully-connected layers of the network to classify the bacteria's clone. Representation and classification networks are trained separately due to a large number of patches per image.

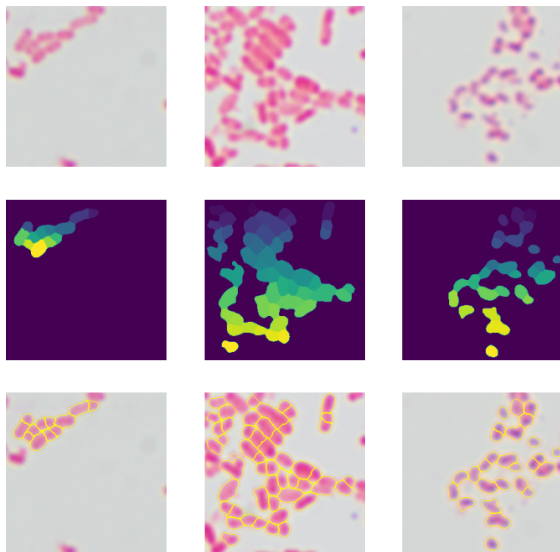


Figure 5: Sample patches (first row) and segments obtained with CellProfiler (second row). The third row shows images with boundaries between labeled regions highlighted.

a result, every connected component, a cycle, or a higher dimensional void can be characterized by a pair of numbers, b and d , the birth and death time. Therefore, a set of birth-death pairs is obtained, called a persistence diagram or persistence barcode. They are not easy to compare due to their variable size. Therefore, we apply a vectorization method called persistence bag of words [18, 19] to obtain a fixed-size representation for each patch. Based on them, we calculate the average persistence bag of words for each clone, e.g., C_1 and C_2 for first and second clones. Then, we obtain the set of features $\{f_i\}_i$ for which there is a significant difference between C_1 and C_2 (see Fig. 13). Finally, we search for the patches P with a persistence bag of word

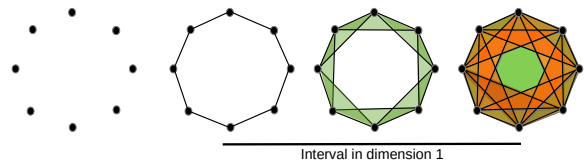


Figure 6: Successive sub-level sets for eight points sampled from a circle. Initially, for a sufficiently small radius, only separate vertices exist. However, when c grows, more and more edges are added. Finally, the topology of a circle is visible almost in all filtration stages. Therefore, it will be recovered by persistence homology in dimension 1 (depicted by the long bar below the picture). Image copied from [19].

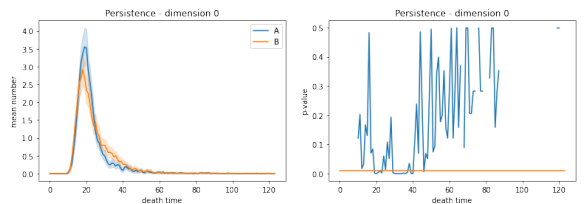


Figure 7: The average persistence bag of words for clones A and B from configuration $A-B$ together with 0.99 confidence interval (left plot). The significance of difference is presented in the right plot with a p-value of 0.01 marked as the orange line. The set of features $\{f_i\}_i$ from Equation 2 corresponds to values below this line. Similar plots for configurations $A-D$ and $B-D$ are available in supplementary materials.

C_P closer to C_1 and farther from C_2 in features $\{f_i\}_i$:

$$R_1 = \arg \min_P \sum_{f_i} |C_P[f_i] - C_1[f_i]| - |C_P[f_i] - C_2[f_i]|. \quad (2)$$

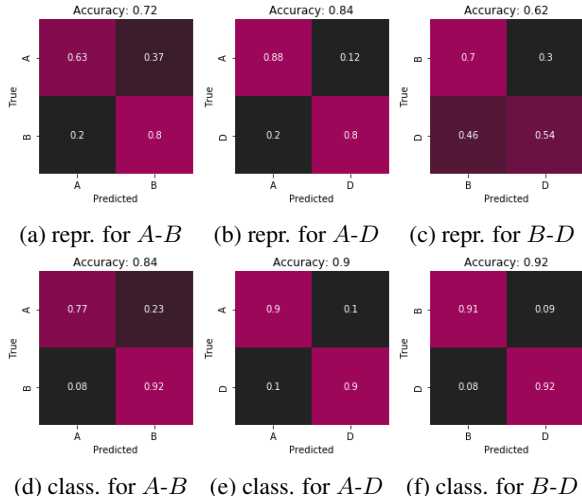


Figure 8: Test confusion matrices for representation and classification networks (first and second row, respectively) averaged over 5 folds. Successive columns correspond to configurations $A-B$, $A-D$, and $B-D$. Train confusion matrices are available in supplementary materials.

We treat them as representative patches of the first clone. The representative patches for the second clone are obtained analogously.

Properties of individual bacteria. To understand what differentiates individual cells between the clones, we limit segments obtained from CellProfiler to those isolated from the others (with no adjacent segments). For them, we analyze significant differences between distributions of size, shape, and color.

5. Experiment setup

We divide the database into 5 folds, each containing 2 or 3 isolates per clone. To increase results’ interpretability, we do not train one classifier for all 3 clones, but instead, we consider 3 configurations for pairs $A-B$, $A-D$, and $B-D$. We train the representation network and classification network 5 time using cross-validation to obtain reliable results for each configuration.

The representation network is finetuned with batch size 64 and initial learning rate 0.0001, decreasing 10 times after every 1000 step (hyperparameters obtained with preliminary experiments). All network layers are finetuned with cross-entropy loss and weighted sampling to reduce the influence of data imbalance. It was trained for 5000 iterations when the loss function flattened.

To obtain the best hyperparameters for the classification network we applied grid search over learning rate in [0.001, 0.0005, 0.0001, 0.00005, 0.00001, 0.000005] and

and weight decay in [0.05, 0.01, 0.005, 0.001, 0.00005, 0.00001]. We use a standard number of attention heads (3) as according to [10] this parameter is not relevant.

When it comes to interpretability, we build the Vietoris-Rips complex from the distance matrix, based on which we then calculate persistence homology of dimension 0 using the Gudhi library [16]. Based on persistence diagrams, we generate a persistence bag of words with regular codewords of size 1.

We performed all the experiments on a workstation with two 23 GB GPU and 128 GB RAM. On average, it takes 30 hours to train a patch representation network and 8 hours to generate patch representations for the classification step. Training of image classification network lasts up to 1 hour. Both networks were implemented using PyTorch. The code is publicly available.⁴

6. Results and discussion

The confusion matrices averaged over 5 folds for patch representation and image classification network are presented in Fig. 14. They clearly indicate that it is possible to differentiate between bacteria clones based only on microscopic images with high accuracy. Moreover, while patch-based test accuracy can be relatively low (0.62 and 0.72 in case of $B-D$ and $A-B$ configurations), it is compensated by attention-based pooling, resulting in the accuracy of image-based classification at the level of 0.9. The image-based accuracy is lower when distinguishing between clones A and B . However, it is expected because they are genetically more similar than clone D (see Fig. 3). As a baseline, we also tested the method used to classify bacteria species based on microscopic images [20]. However, the test accuracy obtained by this method was below 0.7 in all three cases.

We also present quantitative test confusion matrices obtained by representation and classification networks (see Fig. 16). While some trends are visible in the case of representation networks, such as the more scattered distribution of clone B , no systematic characteristic can be implicated, which is in line with the motivation to apply more sophisticated interpretability methods.

As described in Section 4, to interpret AbMIL, we pass a patch through CellProfiler to obtain one segment per cell (see Fig. 5). Then, we generate a point cloud containing centers of the segmented cells to analyze their spatial arrangement and describe the properties of individual cells using segments isolated from the others. The representative patches obtained with the method based on persistence homology (described in Section 4) are presented in Fig. 10. One can observe that clone D is more compact what can be caused by smaller polysaccharide bacterial capsule than in

⁴We will add the link to the code after paper acceptance.

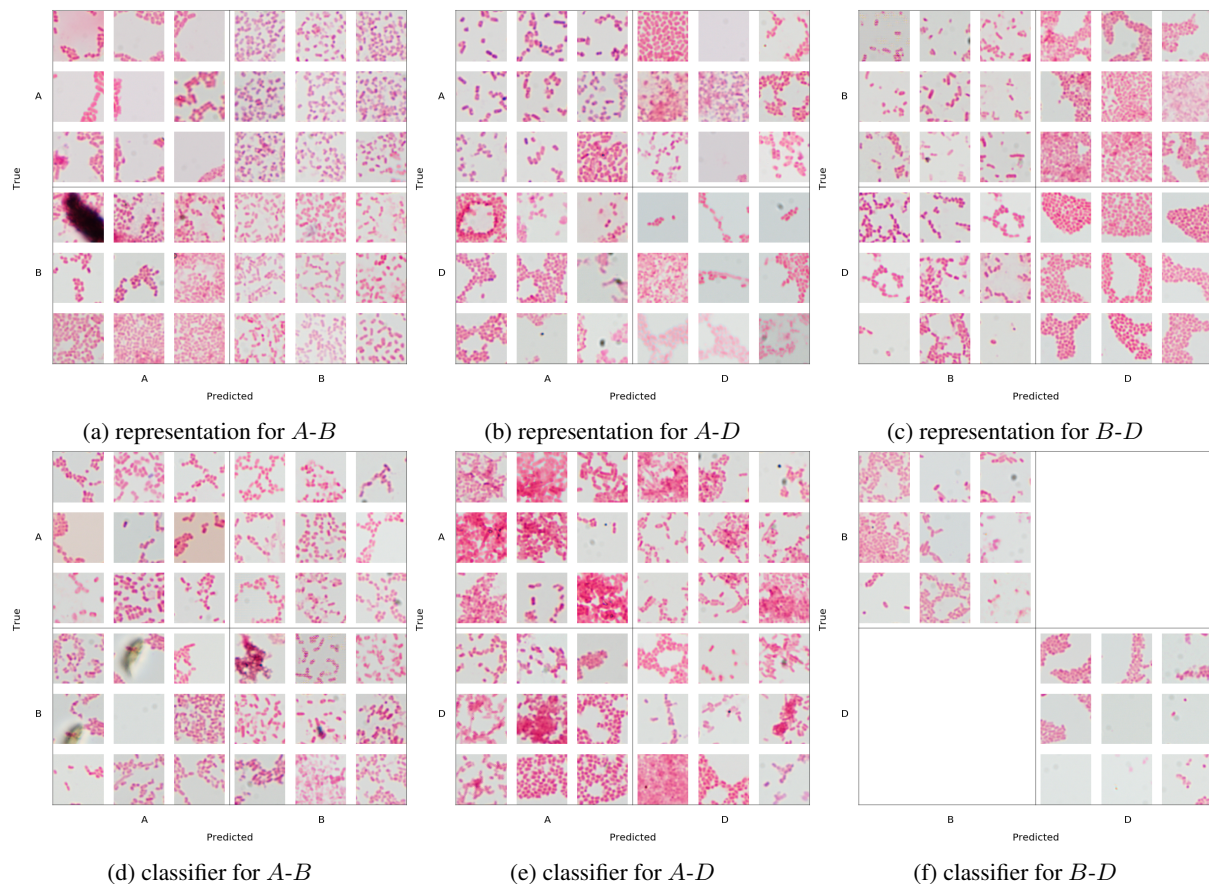


Figure 9: Qualitative test confusion matrices obtained from representation and classification networks (first and second row, respectively) for fold 1, where successive columns correspond to configurations $A-B$, $A-D$, and $B-D$. Each confusion matrix cell contains 9 (3×3) representative patches coming from different images. One can observe no misclassifications in the test set of the considered fold for $B-D$ classification network (bottom-right confusion matrix).

the case of clones A and B (this hypothesis needs further investigation). Moreover, clone B is more scattered than clone A . Interestingly, it results in completely different representatives of clone A in $A-B$ and $A-D$ configurations. In $A-B$, AbMIL expects a compact structure of A , while in $A-D$, the expectations are opposite.

The representative patches from Fig. 10 also suggest other, more individual properties of the bacteria, such as the larger size of bacterial cells from clones A and B comparing to clone D . However, to analyze it systematically, we prepared the statistics for isolated segments from all the patches in Fig. 11. One can observe that bacterial cells of clone A are larger and darker than in clones B and D . Moreover, bacterial cells of clone A is also significantly rounder than in clone B . Simultaneously, bacterial cells of clone D are brighter than in clones A and B . We present a summary of the clones' properties in Fig. 1. We hypothesize that it again can be caused by the presence of a polysaccharide capsule (envelope). More precisely, the thicker capsule

results in: (i) darker color caused by catching more dye during staining; (ii) rounder shape caused by the limited ability to reshape; (iii) larger size due to accumulating dye by both the cell and the envelope.

7. Conclusion

In this paper, we analyzed if it is possible to distinguish between different clones of the same bacteria species (*Klebsiella pneumoniae*) based only on microscopic images. For this challenging task, previously considered impossible, we applied a multi-step algorithm with attention-based multiple instance learning (AbMIL), which resulted in accuracy at the level of 0.9. Moreover, we pointed out the AbMIL interpretation's weaknesses, and we introduced more efficient interpretability methods based on CellProfiler segmentation and persistence homology.

The extensive analysis revealed systematic differences between the clones from the spatial arrangement and the individual cell perspective. Such differences may be caused

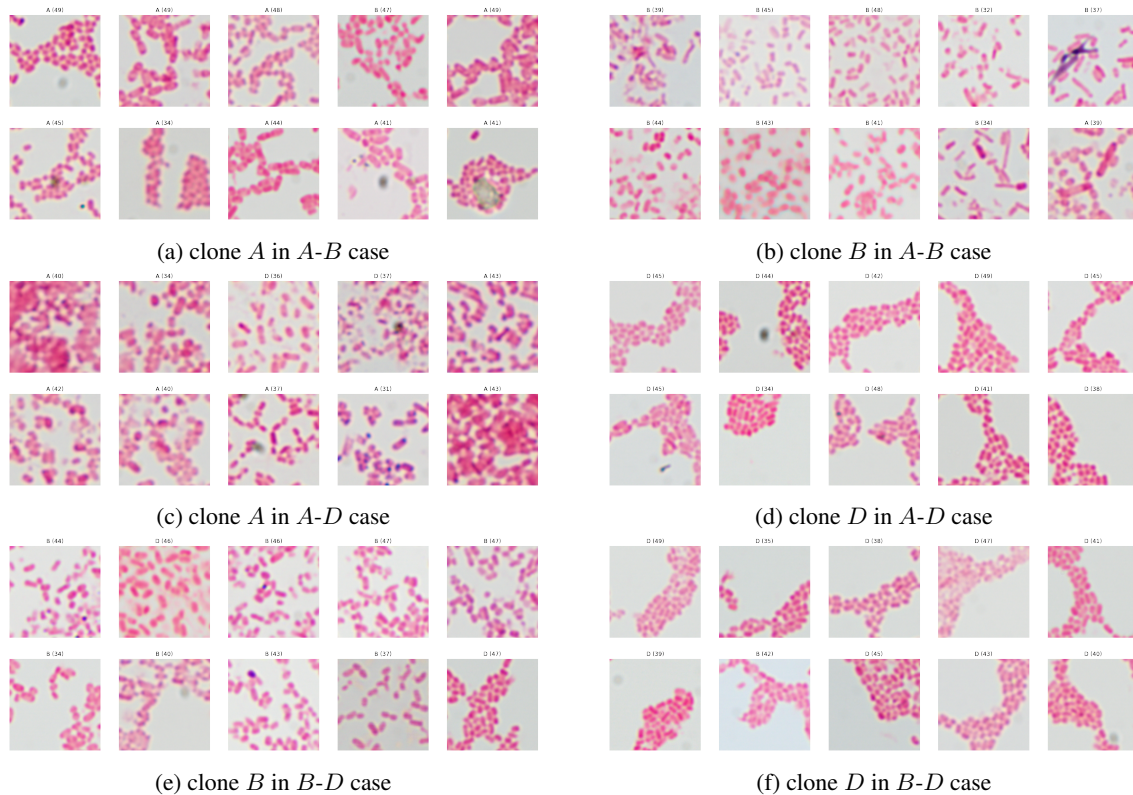


Figure 10: Representative patches of clones obtained for all three configurations (A - B , A - D , and B - D). One can observe that patch representatives of A highly depend on the configuration, as it is less scattered than B but more scattered than D .

by the variance of polysaccharide bacterial capsules' thickness. However, this hypothesis needs further microbiological investigation.

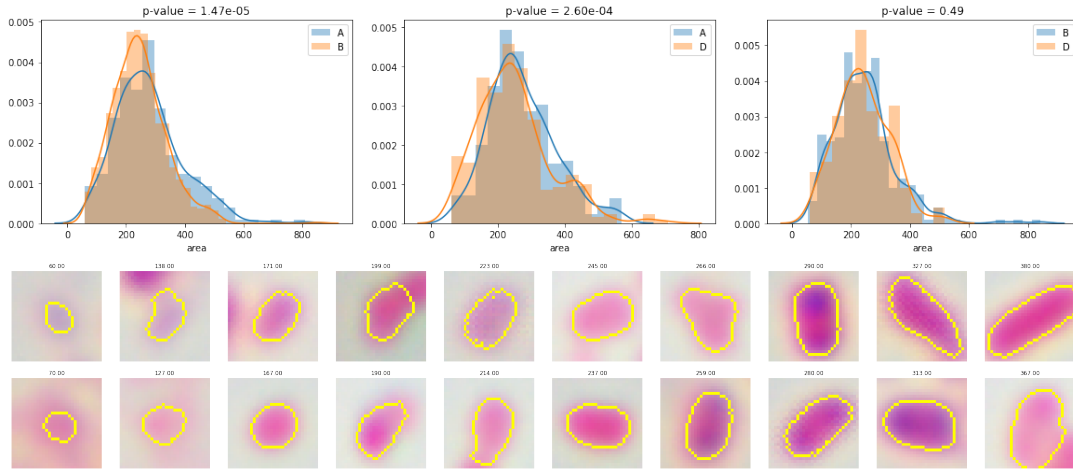
Although the results are extremely promising, the method needs further investigation with a larger number of isolates and clones. Moreover, we plan to investigate if it can be used to predict genetic PFGE profiles.

References

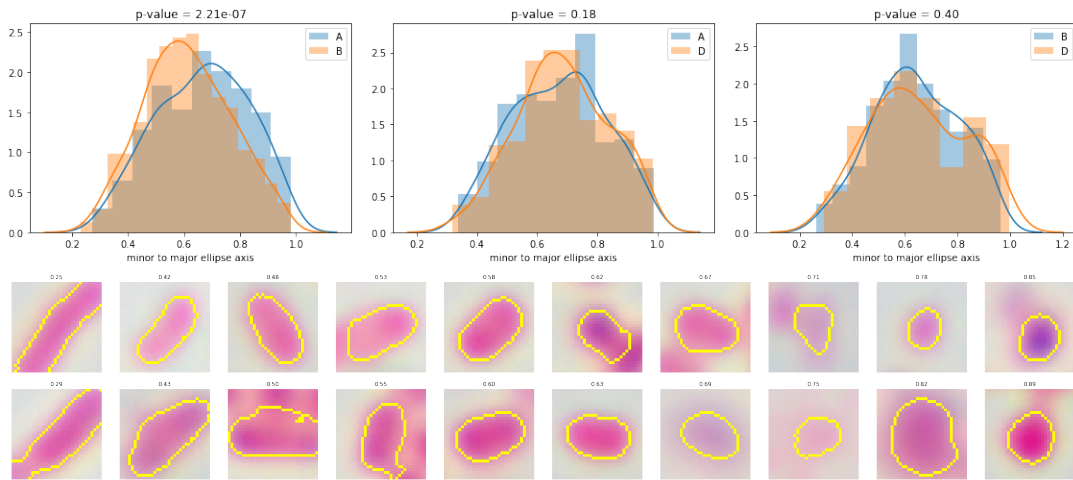
- [1] Simona Bratu, David Landman, Robin Haag, Rose Recco, Antonella Eramo, Maqsood Alam, and John Quale. Rapid spread of carbapenem-resistant klebsiella pneumoniae in new york city. *Archives of Internal Medicine*, 165(12):1430, June 2005. [1](#)
- [2] Anne E Carpenter, Thouis R Jones, Michael R Lamprecht, Colin Clarke, In Han Kang, Ola Friman, David A Guertin, Joo Han Chang, Robert A Lindquist, Jason Moffat, et al. Cellprofiler: image analysis software for identifying and quantifying cell phenotypes. *Genome biology*, 7(10):R100, 2006. [2](#), [3](#)
- [3] L. Diancourt, V. Passet, J. Verhoef, P. A. D. Grimont, and S. Brisse. Multilocus sequence typing of klebsiella pneumoniae nosocomial isolates. *Journal of Clinical Microbiology*, 43(8):4178–4182, Aug. 2005. [1](#)
- [4] Herbert Edelsbrunner, David Letscher, and Afra Zomorodian. Topological persistence and simplification. In *Proceedings 41st annual symposium on foundations of computer science*, pages 454–463. IEEE, 2000. [2](#), [3](#)
- [5] Massimo Ferri. Persistent topology for natural data analysis—a survey. In *Towards Integrative Machine Learning and Knowledge Extraction*, pages 117–133. Springer, 2017. [3](#)
- [6] C-P Fung, F-Y Chang, S-C Lee, B-S Hu, B I-T Kuo, C-Y Liu, M Ho, and L K Siu. A global emerging disease of klebsiella pneumoniae liver abscess: is serotype k1 an important factor for complicated endophthalmitis? *Gut*, 50(3):420–424, 2002. [2](#)
- [7] Hui Han, Haijian Zhou, Haishan Li, Yuan Gao, Zhi Lu, Kongxin Hu, and Baoliang Xu. Optimization of pulse-field gel electrophoresis for subtyping of klebsiella pneumoniae. *International Journal of Environmental Research and Public Health*, 10(7):2720–2731, July 2013. [1](#)
- [8] Kaiming He, Xiangyu Zhang, Shaoqing Ren, and Jian Sun. Deep residual learning for image recognition. *CoRR*, abs/1512.03385, 2015. [3](#)
- [9] Maximilian Ilse, Jakub Tomczak, and Max Welling. Attention-based deep multiple instance learning. In Jennifer Dy and Andreas Krause, editors, *Proceedings of the 35th International Conference on Machine Learning*, volume 80 of *Proceedings of Machine Learning Research*, pages 2127–

2136, Stockholmsmässan, Stockholm Sweden, 10–15 Jul 2018. PMLR. [3](#)

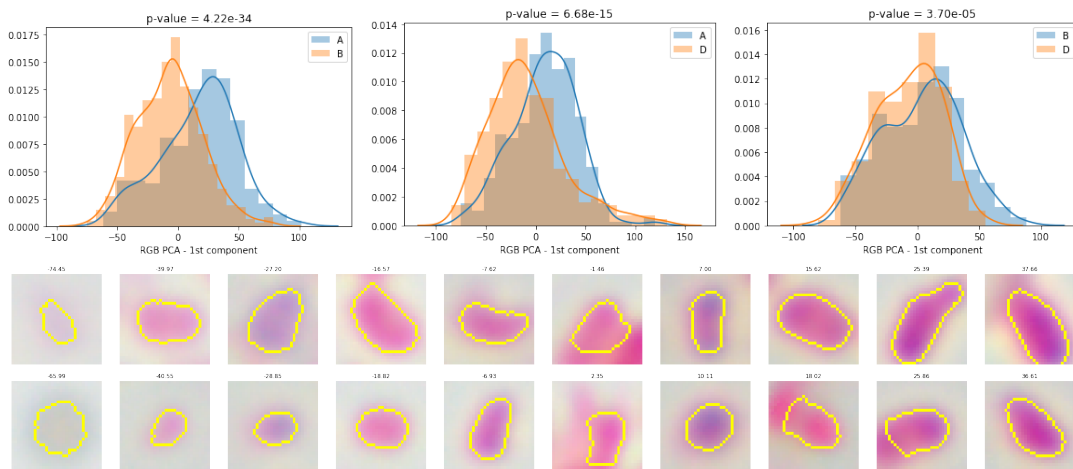
- [10] Maximilian Ilse, Jakub M Tomczak, and Max Welling. Attention-based deep multiple instance learning. In *35th International Conference on Machine Learning, ICML 2018*, pages 3376–3391. International Machine Learning Society (IMLS), 2018. [2](#), [3](#), [5](#)
- [11] Daniel Jonas, Bettina Spitzmüller, Franz D. Daschner, Jan Verhoef, and Sylvain Brisse. Discrimination of klebsiella pneumoniae and klebsiella oxytoca phylogenetic groups and other klebsiella species by use of amplified fragment length polymorphism. *Research in Microbiology*, 155(1):17–23, Jan. 2004. [1](#)
- [12] Edison Mutsinzi Karama, François Willermain, Xavier Janssens, Marc Claus, Sigi Van den Wijngaert, Jim-Town Wang, Claire Verougstraete, and Laure Caspers. Endogenous endophthalmitis complicating klebsiella pneumoniae liver abscess in europe: case report. *International Ophthalmology*, 28(2):111–113, Aug. 2007. [2](#)
- [13] Wen-Chien Ko. Community-acquired klebsiella pneumoniae bacteremia: Global differences in clinical patterns. *Emerging Infectious Diseases*, 8(2):160–166, Feb. 2002. [2](#)
- [14] Y. J. Lau, B. S. Hu, W. L. Wu, Y. H. Lin, H. Y. Chang, and Z. Y. Shi. Identification of a major cluster of Klebsiella pneumoniae isolates from patients with liver abscess in Taiwan. *J. Clin. Microbiol.*, 38(1):412–414, 1 2000. [1](#)
- [15] K. Mamlouk, I. Boutiba-Ben Boubaker, V. Gautier, S. Vimont, B. Picard, S. Ben Redjeb, and G. Arlet. Emergence and outbreaks of CTX-m β -lactamase-producing escherichia coli and klebsiella pneumoniae strains in a tunisian hospital. *Journal of Clinical Microbiology*, 44(11):4049–4056, Sept. 2006. [1](#)
- [16] Clément Maria, Jean-Daniel Boissonnat, Marc Glisse, and Mariette Yvinec. The gudhi library: Simplicial complexes and persistent homology. In *International Congress on Mathematical Software*, pages 167–174. Springer, 2014. [5](#)
- [17] Dawid Rymarczyk, Jacek Tabor, and Bartosz Zieliński. Kernel self-attention in deep multiple instance learning. *arXiv preprint arXiv:2005.12991*, 2020. [3](#)
- [18] Bartosz Zieliński, Michał Lipiński, Mateusz Juda, Matthias Zeppelzauer, and Paweł Dłotko. Persistence bag-of-words for topological data analysis. In *Proceedings of the 28th International Joint Conference on Artificial Intelligence*, pages 4489–4495. AAAI Press, 2019. [4](#)
- [19] Bartosz Zieliński, Michał Lipiński, Mateusz Juda, Matthias Zeppelzauer, and Paweł Dłotko. Persistence codebooks for topological data analysis. *Artificial Intelligence Review*, pages 1–41, 2020. [4](#)
- [20] Bartosz Zieliński, Anna Plichta, Krzysztof Misztal, Przemysław Spurek, Monika Brzywczy-Włoch, and Dorota Ochońska. Deep learning approach to bacterial colony classification. *PloS one*, 12(9):e0184554, 2017. [2](#), [5](#)



(a) distribution of size



(b) distribution of roundness



(c) distribution of darkness

Figure 11: Distributions of size (a), roundness (b), and darkness (c) for all three configurations (presented in three successive columns), as well as sample bacteria cells from the lowest (left side) to the highest value (right side) of considered properties.

In these supplementary materials, we first present additional sample images from the DIBaC database (see Fig. 12). We also present the average persistence bag of words for configurations $A-D$ and $B-D$ (see Fig. 13). Moreover, we present standard and qualitative train confusion matrices obtained from representation and classification networks (see Fig. 14 and 16). For the latter network, we additionally deliver receiver operating characteristics (see Fig. 15). Finally, we present the statistics on the number of bacteria and the number of connected components in AbMIL crucial patches (see Fig. 17).

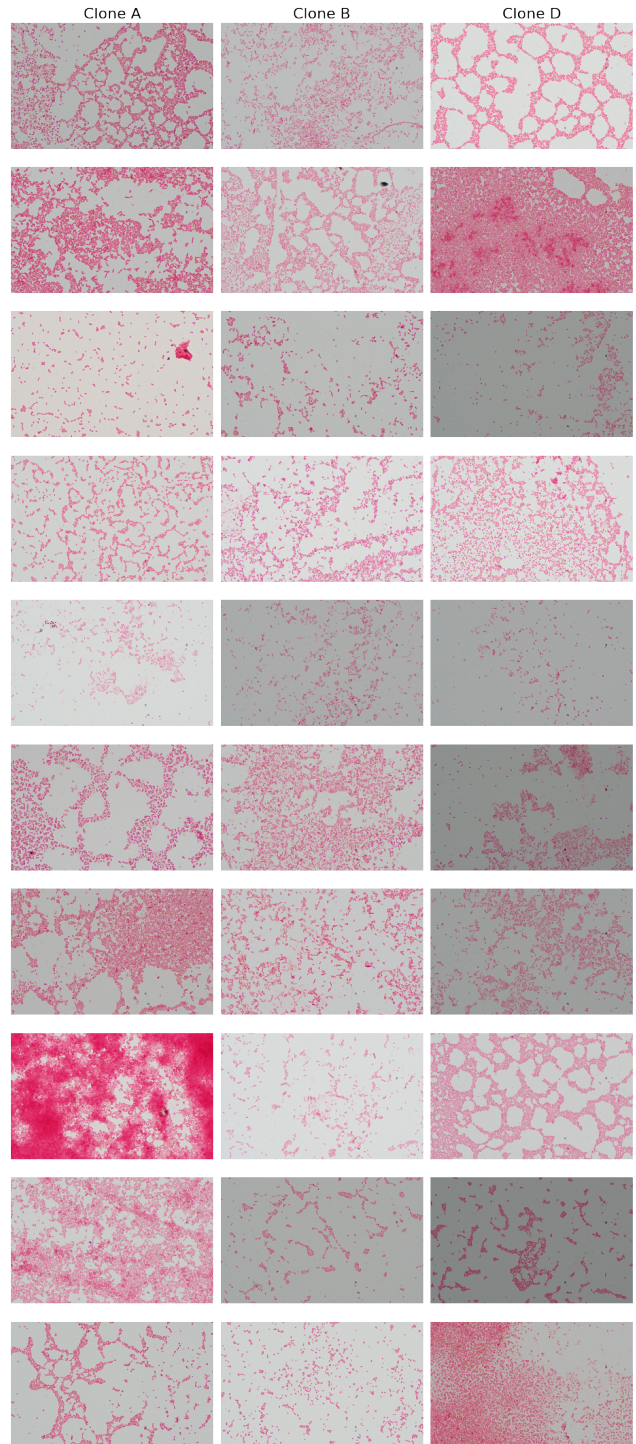
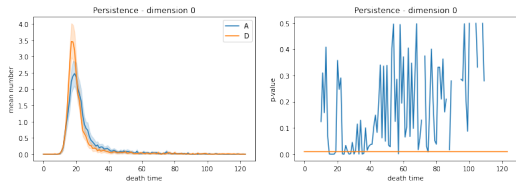
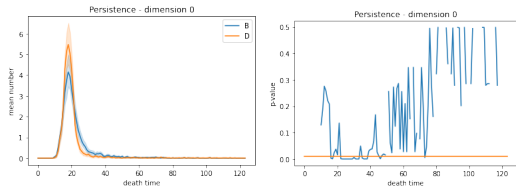


Figure 12: Sample images from the DIBaC database (10 per clone).

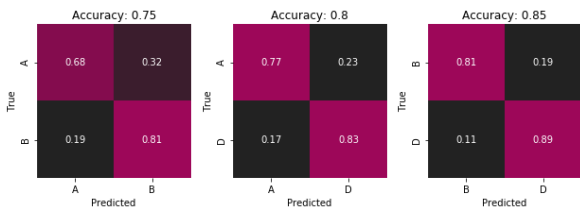


(a) configuration *A-D*

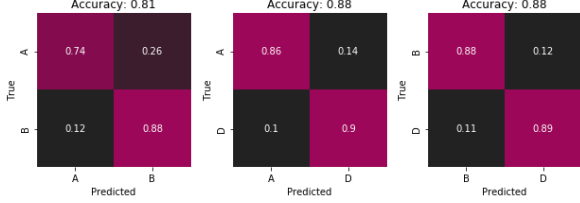


(b) configuration *B-D*

Figure 13: The average persistence bag of words for configurations *A-D* and *B-D* together with 0.99 confidence interval (first column). The significance of difference is presented in the right column with a p-value of 0.01 marked as the orange line.

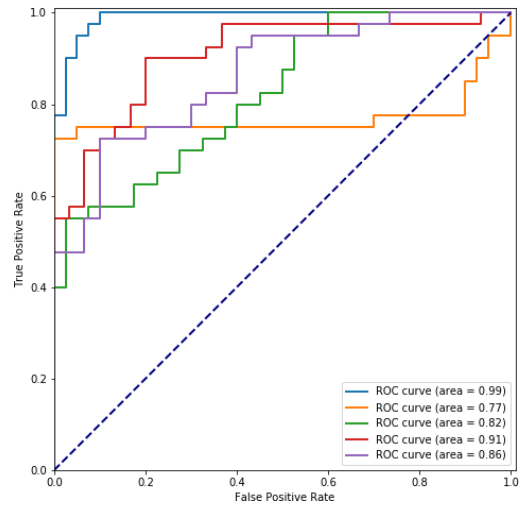


(a) repr. for *A-B* (b) repr. for *A-D* (c) repr. for *B-D*

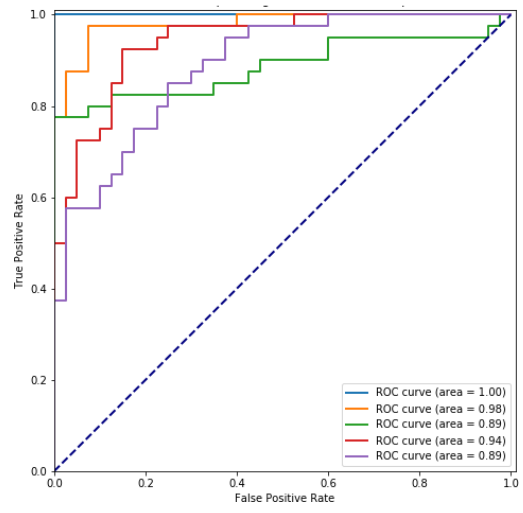


(d) class. for *A-B* (e) class. for *A-D* (f) class. for *B-D*

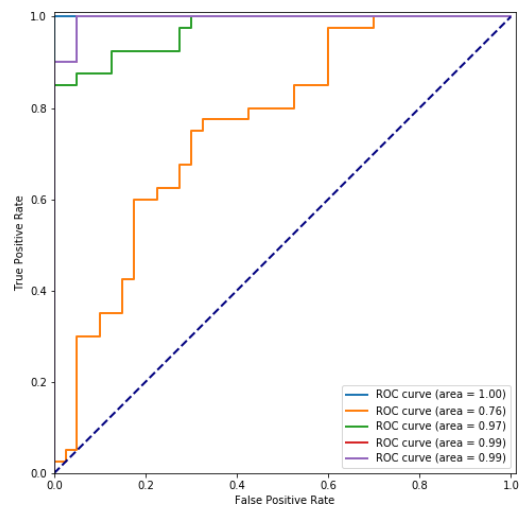
Figure 14: Train confusion matrices for representation and classification networks (first and second row, respectively) averaged over 5 folds. Successive columns correspond to classifiers *A-B*, *A-D*, and *B-D*.



(a) classifier *A-B*



(b) classifier *A-D*



(c) classifier *B-D*

Figure 15: Receiver operating characteristics (ROC) curves for each fold of AbMIL models.

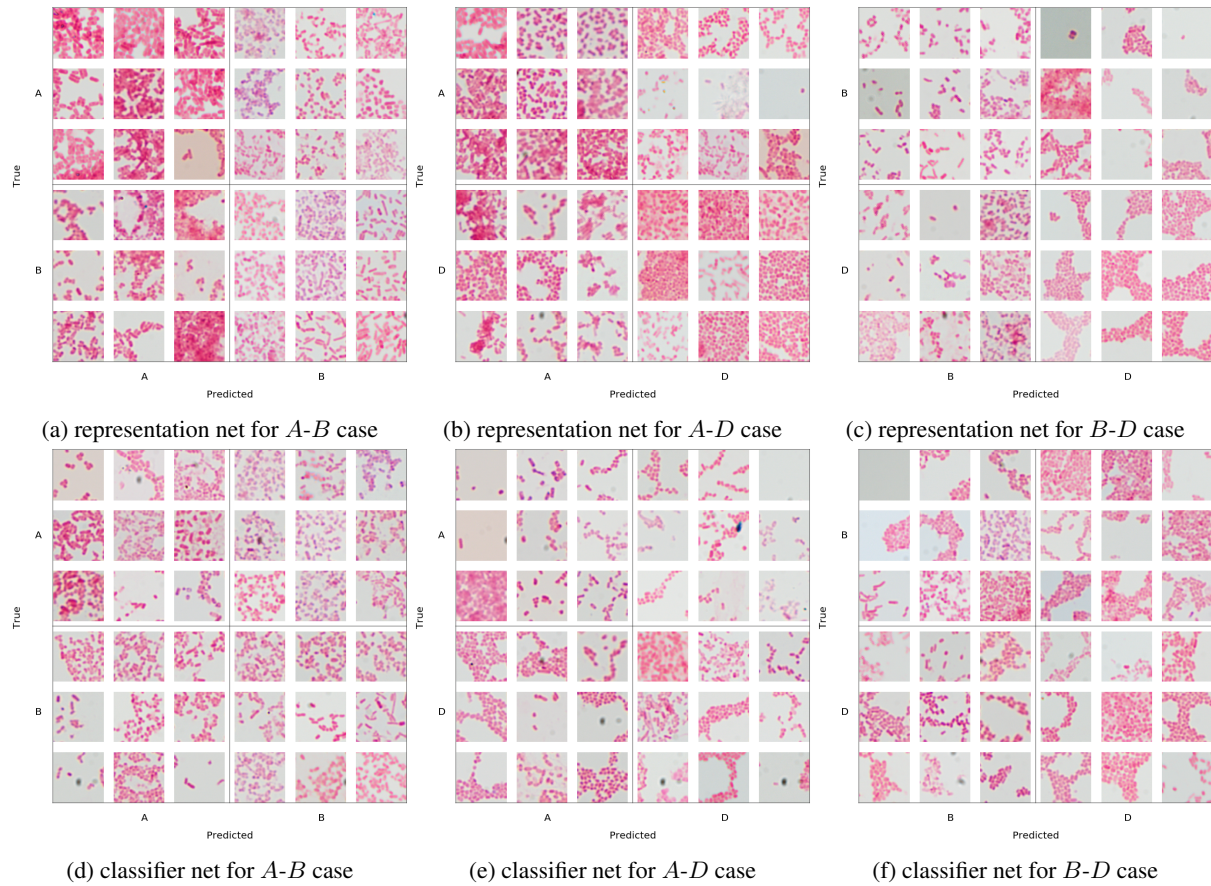
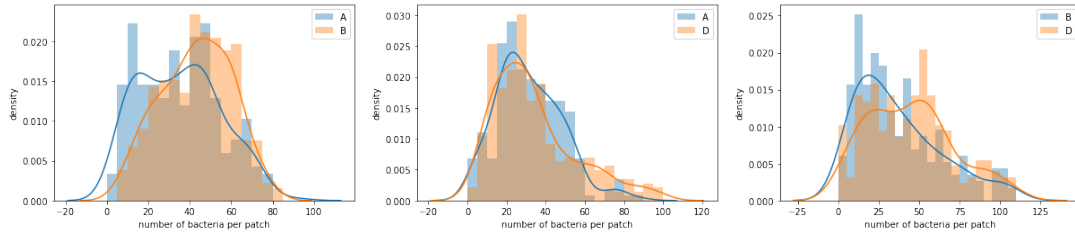
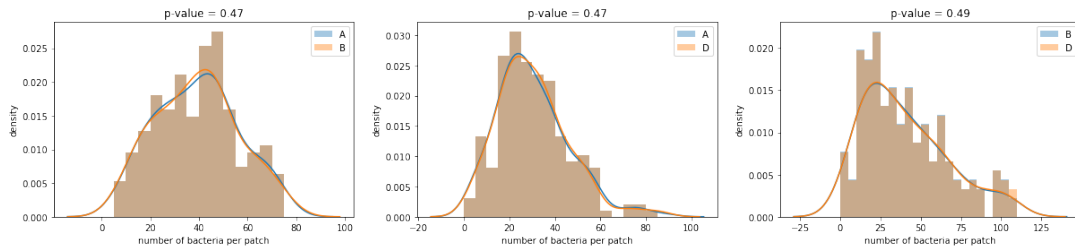


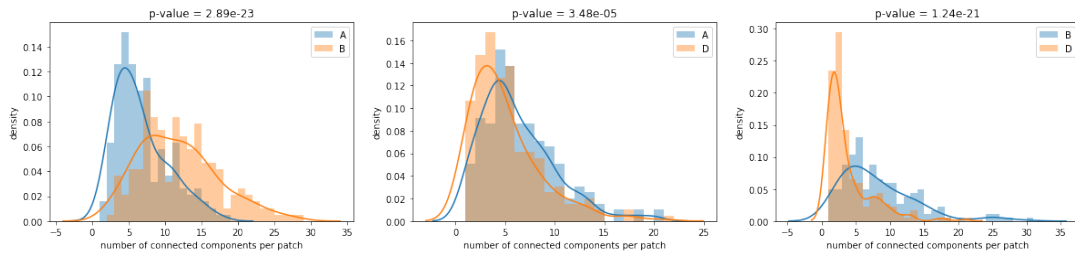
Figure 16: Qualitative train confusion matrices obtained from representation and classification networks (first and second row, respectively) for fold 1, where successive columns correspond to configurations $A-B$, $A-D$, and $B-D$. Each confusion matrix cell contains 9 (3×3) representative patches coming from different images.



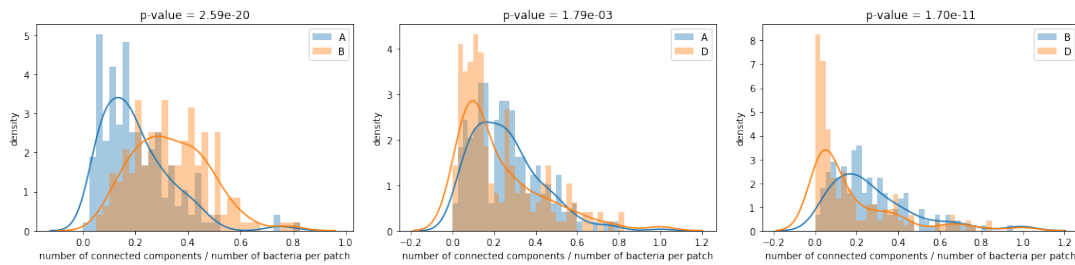
(a) number of bacteria per patch



(b) number of bacteria per patch (same number of patches per bin for each clone)



(c) number of connected components per patch limited to patches from (b)



(d) number of connected components / number of bacteria per patch limited to patches from (b)

Figure 17: Statistics on the number of bacteria and the number of connected components in AbMIL crucial patches. Successive columns correspond to classifiers A - B , A - D , and B - D .